Materials Advances

ROYAL SOCIETY OF CHEMISTRY

PAPER

View Article Online
View Journal | View Issue

Open Access Article. Published on 06 October 2025. Downloaded on 1/21/2026 7:21:53 AM.
This article is licensed under a Creative Commons Attribution 3.0 Unported Licence.

Check for updates

Cite this: *Mater. Adv.*, 2025, **6**, 7996

Pioneering bio-derived greener and sustainable Cu/biochar nanoplates for expedient adsorption of DR 227 dye

Amna Sanaullah,[a] Sadia Muzammal,[b] Awais Ahmad,*[c] Sadia Ata,*[d] Raziya Nadeem,[a] Maryam Sana,[a] Mohammed Habila[c] and Ghulam Mustafa*[ac]

Received 4th July 2025,
Accepted 21st July 2025

DOI: 10.1039/d5ma00705d

rsc.li/materials-advances

The present work reports a comparative study of fish scale biomass (FSBM), fish scale biochar (FSBC), acid treated fish scale biochar (ATFSBC), and a nano Cu-acid treated fish scale biochar composite (Cu/FS NCs), synthesized by using *Punica granatum* as a reducing and capping agent. All the experiments were performed in a batch process where the effect of pH (1.0–10.0), dose rate (0.05–0.1 g), dye initial concentration (10–150 ppm), and contact time (24 hours) were investigated for maximum adsorption of Direct Red (DR) 227 dye. Results showed that the Cu/FS NC adsorbent has the maximum degradation of DR-227 dye, *i.e.*, 99.99% was found among all adsorbents. The highest value of q_e (mg g^{-1}) for Cu/FS NCs was obtained at optimum pH 2, dose rate 0.05 g, contact time 240 min, and concentration 120 ppm. The Freundlich model and the pseudo-second-order model match the dye adsorption process of DR-227. The reusability of Cu/FS NCs was maintained through cyclic testing, revealing negligible degradation in catalytic activity. Further identification of the material properties was achieved through SEM analysis, and it showed that the adsorbent was obtained in nanoplate form. Furthermore, FTIR spectra of the adsorbent were a clear indication of the formation of the material. So, the current study proposes that biomass-derived Cu nanoplates can be useful in targeting sustainability threats.

1. Introduction

Water is one of the central natural assets on Earth for all living entities. All fundamental processes of the biosphere rely upon the accessibility of water, and a significant portion of water is utilized for modern industrial cycles. Among various enterprises, textile businesses use a colossal amount of water in various processes such as coloring and washing, and the resulting untreated water is a risk.[1] Aquatic water is polluted by dyes eliminated from industries such as pharmaceuticals, tanneries, plastic, electroplating, *etc.* Dyes are recalcitrant organic compounds that remain unaffected by chemical and biological attack due to their synthetic derivation and complex structure.[2–4] It is reported that around 40–65 liters of wastewater are produced after coloring 1 kg of textile fabric. In the dying process, roughly 20% of various dyes are lost. Commercially used reactive dyes have chromophoric groups such as triphenylmethane and azo,[5] which are a significant threat to the biosphere, and have numerous cancer-causing and mutagenic effects when eliminated with waste runoffs.[6,7] Textile industry effluents, if left untreated, can severely impact the environment by altering pH balances, increasing suspended solids, and elevating BOD, COD, and coliform bacteria levels, compromising water quality and ecological health.[8,9] In this way, colored wastewater is a danger to the natural balance, which restricts downstream use like drinking, washing, and irrigation.[9] DR 227 belongs to the azo (–N=N–) group of dyes as shown in Fig. 1, and is used widely used for dyeing cellulose fiber, polyester/cotton, and polyester/stick blends.

Water treatment techniques such as bio-treatment,[10] advanced electrochemical oxidation,[11] catalytic ozonation,[1,12] coagulation,[13] photocatalytic degradation[13–15] and adsorption[16,17] *etc.*, were developed to remove contaminants from aqueous systems. For efficient and sustainable wastewater treatment, researchers have explored the potential of eco-friendly absorbents, including activated charcoal, biological thresholds, and innovative composites like biochar, natural clay, and metal-modified seed husk, offering a cost-effective solution.[18] Adsorbents such as activated carbon,[19,20] natural clay,[21] biochar,[22] algae-lignocellulosic biochar composites,[23] magnetic-carbon composites,[23] silica–alumina composites[24] and metal-modified seed husks[25] have been used in wastewater treatment.[9]

[a] Department of Chemistry, University of Agriculture, Faisalabad, Pakistan. E-mail: Ghulam.mustafa@chem.uol.edu.pk
[b] Department of Environmental Sciences, Government College University, Faisalabad, 38000, Pakistan
[c] Department of Chemistry, University of Lahore, Lahore, Pakistan. E-mail: awaisahmed@gcuf.edu.pk
[d] School of Chemistry, University of Punjab, Lahore, Pakistan

© 2025 The Author(s). Published by the Royal Society of Chemistry

Open Access Article. Published on 06 October 2025. Downloaded on 1/21/2026 7:21:53 AM.
This article is licensed under a Creative Commons Attribution 3.0 Unported Licence.

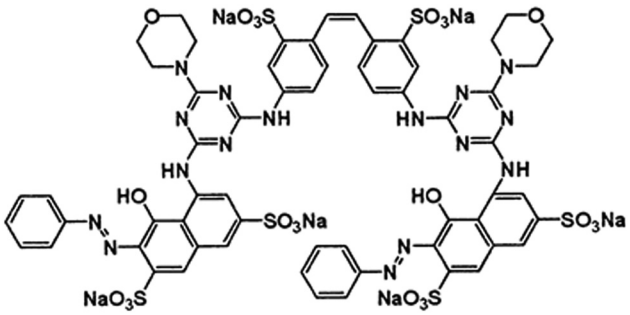

Fig. 1 Direct Red 227.

Green synthesized metal nanoparticles (NPs) with plant extracts are a novel group of materials, utilized for environmental remediation because of their distinctive properties *i.e.* large surface area, small particle size, thermal stability, biocompatibility, and mild reaction conditions *i.e.* without high pressure, temperature, hazardous materials such as surfactant, and capping agents.[26,27] Copper NPs have attained particular importance in many fields because of their electrical conductivity, mechanical, and thermocatalytic properties, and they are cheaper than other noble metals.[28] The major drawbacks of metal NPs are their short lifetime and agglomeration in their catalytic applications. In the solution phase, metal NPs aggregate, causing deactivation of the catalyst due to a decrease in their available surface area. Because of their ion release and solubility, CuO NPs have considerable potential for ecotoxicity, especially in environments that are oxidative or acidic.[29] CuO NPs emit Cu^{2+} ions that can upset aquatic creatures' biological balance when they enter aquatic systems. CuO NPs have been shown to have both acute and long-term harmful effects on aquatic animals, including zebrafish (Danio rerio), *Chlorella vulgaris*, and *Daphnia magna*. These effects include oxidative stress, mitochondrial malfunction, and growth inhibition. Depending on the species and exposure duration, EC50 values can range from 0.5 to 10 mg L^{-1}, suggesting moderate to high toxicity. In addition, CuO NPs considerably reduce wastewater microbial populations by interfering with bacterial cell membranes and enzymes. This could change the ability of natural or artificial ecosystems to biodegrade. Interestingly, Gram-negative bacteria are more susceptible than Gram-positive bacteria. Through foliar or root uptake, CuO NPs can also adversely impact plants, resulting in oxidative stress, growth inhibition, and decreased photosynthetic efficiency.[30,31] For plants like *Lactuca sativa*, *Triticum aestivum*, and *Zea mays*, high concentrations (usually >50 mg L^{-1}) might prevent seed germination, root elongation, and chlorophyll content. Production of ROS (reactive oxygen species), which harm DNA and membranes, the buildup of Cu^{2+} ions in plant tissues, and disturbance of hormone signaling and food absorption also occur.[32] Nevertheless, because of their micronutrient function (Cu being necessary in trace amounts), low concentrations of CuO NPs (<10 mg L^{-1}) would not be appreciably detrimental and might even promote growth. Moreover, it is also challenging to separate, recover, and reuse metal NPs from reactions. These problems could be sorted by the fabrication of metal NPs on solid prop zeolite, polymer, metal oxides, graphene, magnetic materials, activated carbon, clay minerals, and biochar to form nanocomposites.[27,33,34]

Punica granatum is a powerful fruit considered "a pharmacy unto itself". In the peels of *Punica granatum*, a high concentration of phenolic compounds, and punicalagin, the gallic, ellagic acids, chlorogenic acids, caffeic acids, punicalins, apigenin, quercetin, pelargonidin, and granatin A and B are present and serve as capping and stabilization molecules.[35–38] NPs are loaded onto the solid prop to form nanocomposites, which provide stability and increase the surface area.[39,40] Fish scales are produced as waste by aquaculture zones such as fish salting, canning, filleting, packing, *etc.*, and are dumped at sea and disposed of in landfills. The higher organic constitution present in fish scales is collagen fibers bound through calcium compounds and functional groups, *i.e.*, carbonate, hydroxyl, phosphate, and carboxyl, that possess adsorptive properties. Solid fish scales have been used to produce porous carbon or biochar with high attraction for acidic dye contaminants.[41]

This study presents copper nanoparticle-functionalized biochar (Cu/FS NCs), a unique, green-engineered nanocomposite made from fish scale waste and extracts from the peel of *Punica granatum*. To the best of our knowledge, this is the first report on the effective adsorption of anionic Direct Red 227 dye using Cu-based nanoplates anchored on acid-treated fish scale biochar *via* a phytochemical route. Superior adsorption capacity (476.19 mg g^{-1}) and reusability over several cycles without appreciable performance degradation are exhibited by the resultant Cu/FS NCs. In line with the concepts of green chemistry and the circular economy, this study creates a low-cost, sustainable platform that turns biowaste into cutting-edge functional materials for highly effective wastewater cleanup.

2. Materials and methods

2.1. Preparation of *Punica granatum* peel extract

Fresh pomegranate was collected, peeled, washed, dried, and ground in an electric grinder to form a powder. To prepare the peel extract, 5 g of pomegranate peel powder was mixed with 50 mL of distilled water for 45 min at 80 °C. After filtration, the extract was refrigerated (4–8 °C) and used as a reducing and stabilizing agent for further studies.[42]

2.2. Preparation of biosynthesized CuO NPs

The copper oxide NPs were synthesized by adding a 40 mL extract of pomegranate, and the same volume of 0.09 g of copper(II) chloride dihydrate ($CuCl_2{\cdot}2H_2O$) was dissolved in 100 mL of deionized water for the bioreduction of Cu^{2+} to Cu^0. During the heating process, 1 g of NaOH was added to adjust the pH, and the process of heating was continued until the color of the mixture changed to black, which indicated the formation of CuO NPs. At 4000 rpm, the black aqueous mixture was centrifuged for 20 min and washed for the complete separation of precipitates. The precipitates were washed thoroughly with deionized water and

Open Access Article. Published on 06 October 2025. Downloaded on 1/21/2026 7:21:53 AM.
This article is licensed under a Creative Commons Attribution 3.0 Unported Licence.

hot ethanol and then desiccated at 70 °C in an oven under reflux conditions and kept in air-tight sample bottles.[42,43]

2.3. Preparation of supporting medium for CuO NPs

2.3.1. Preparation of fish scales biomass (FSBM). Fish scales were collected from local shops in Faisalabad, Pakistan. Mixed fish scales were washed and dipped in hot water repeatedly, followed by cold distilled water to remove organic debris from the surface. They were sun-dried for 5 days to remove excess moisture, followed by crisping in an oven at 80 °C. Then, the crisped scales were ground and sieved to obtain a fine, homogenous particle size of bioadsorbent. The fractions were well-preserved in polyethylene bags for use in subsequent experiments.[44,45]

2.3.2. Preparation of fish scale biochar (FSBC). The fish scales were placed in a stainless-steel crucible and subjected to carbonization in an electrical furnace at 550 °C for 90 min. After carbonization, the carbonized fish scales were cooled at room temperature.[46,47]

2.3.3. Acidic treatment of fish scale biochar (ATFSBC). Carbonized fish scales were washed with 1 M HCl solution to remove residual inorganic impurities and to open the pores, and then dipped in hot distilled water to neutralize the biochar. The synthesized biochar underwent oven drying at 100 °C for 12 hours, followed by grinding and sieving to produce fine particles.[46]

2.3.4. Preparation of Cu/fish scale nanocomposites (Cu/FS NCs). In a 500 mL conical flask, after acidic treatment of fish scale biochar, 3.0 g of a dried powder of fish scale biochar and 0.3 g of copper NPs were mixed with 150 mL of distilled water under reflux conditions for 24 h until CuO NPs were fabricated on the support and Cu/fish nanocomposites were formed. The synthesized Cu/fish scale nanocomposites were filtered and dehydrated in an oven at 50 °C for an hour.[42]

2.4. Characterization of the biosynthesized adsorbents

The successful green synthesis of CuO NPs was confirmed using ultraviolet-visible (UV-vis) spectroscopy. This technique allowed for the analysis of the reaction mixture across a wavelength range of 300–800 nm, enabling the identification of the maximum absorption spectra of the samples. The UV-vis spectrophotometer requires only a small sample amount for analysis, minimizing interference. To visualize the surface morphology of the biosynthesized Cu-fish scale nanocomposites, scanning electron microscopy (SEM) was employed. SEM involves scanning the sample surface with a beam of electrons, which interact with the sample's atoms to produce images at various magnifications. These magnified images provided valuable information on the shape and surface topography of the nanocomposites, both before and after the adsorption process. Fourier-transform infrared spectroscopy (FTIR) was utilized to identify the functional groups and biomolecules acting as capping and stabilizing agents for the copper NPs. The dried powder of biosynthesized Cu-NPs, fish scale biomass, fish scale biochar, acid-treated fish scale biochar, and DR 227 dye-loaded samples were analyzed using FT-IR. The resulting IR absorption spectra, obtained within the range of 4000–500 cm^{-1}, served as molecular fingerprints, revealing the types of chemical bonds present in the molecules.[9,48] Energy-dispersive X-ray spectroscopy (EDS) was employed for the chemical characterization and elemental analysis of the biosynthesized Cu/Fish scale nanocomposites. This technique exploits the unique electromagnetic emission spectrum of each element, producing distinctive peaks that facilitate the identification.[49]

2.5. Batch adsorption systems

Adsorption experiments were carried out in a batch reactor system. Experiments were done to explore the adsorbent ability of FSBM and FSBC. ATFSBC and Cu/FS NCs. Experimental solutions were synthesized by using a stock solution of 1000 ppm. To investigate the effect of pH (1–10), contact time (0–1440 min), dose rate (0.05–0.1 g), and different concentrations (10–100 mg L^{-1}), adsorbents (FSBM, FSBC, ATFSBC, and Cu/FS NCs) along with 50 mL of dye solution were shaken in an orbital shaker at 120 rpm at ambient temperature. 0.1 M NaOH or 0.1 M H_2SO_4 was utilized to prepare the solutions of various pHs. In a batch reactor system, adsorbents such as fish scale biomass, fish scale biochar, acid-treated fish scale biochar, and Cu/Fish scale nanocomposites (FSBM, FSBC. ATFSBC, and Cu/FS NCs) were added and kept in the shaker for a day to attain equilibrium, after which the residue was filtered through filter paper. The remaining amount of dye in the aqueous solution was examined using a UV/VIS spectrophotometer at a wavelength of 550 nm. Experiments under similar conditions for the blank were run in parallel, except for the addition of adsorbents.

2.6. Adsorption studies

2.6.1. Adsorption efficiency. The efficiency of the synthesized adsorbent for the removal of dyes can be evaluated through its adsorption capacity q_e (mg g^{-1}) and percentage adsorption (%), and can be assessed by the given relationships:

$$q_e = (C_0 - C_e)\frac{V}{W}$$

where C_0 (mg L^{-1}) and C_e (mg L^{-1}) are the initial concentration and concentration at equilibrium and V (L) is the volume of solution and W (g) is the mass of adsorbent.

$$\%\ \text{removal} = \frac{C_i - C_e}{C_i} \times 100$$

where C_i and C_e are the initial and final concentrations of the dye in solution (mg L^{-1}).

$$C_e = \text{absorbance} \times \text{S.F.}$$

S.F. is a standard factor that can be calculated using a calibration curve. The absorbance of an aqueous solution containing DR 227 dye was measured at a wavelength of 550 nm.

2.7. Statistical analysis

At 5% probability, one-way ANOVA was used to analyse the data with IBM SPSS Statistics for Windows, version 21.0. The multiple comparisons of means were performed with Tukey's HSD *post hoc* test.

 © 2025 The Author(s). Published by the Royal Society of Chemistry

Open Access Article. Published on 06 October 2025. Downloaded on 1/21/2026 7:21:53 AM.
This article is licensed under a Creative Commons Attribution 3.0 Unported Licence.

3. Results and discussion

3.1. Material characterization

3.1.1. FTIR analysis. FTIR spectroscopy is used to determine the vibrational characteristics of different polymeric, organic, and inorganic functional groups present in a substance. Infrared rays interact with the sample, which causes the stretching, contracting, and bending of chemical bonds. Consequently, IR rays were adsorbed by functional groups in a definite wavelength range irrespective of the structure of the remaining molecules. Literature suggests that intermolecular interactions, specifically hydrogen bonding between the adsorbent and adsorbate, as well as surface charge modifications resulting from protonation and deprotonation of functional groups on the adsorbent, contribute to the adsorption of the dye. FTIR spectra of FSBM, FSBC, ATFSBC, and Cu/FS NCs were obtained before and after adsorption of DR 227. FTIR spectra of green synthesized Cu-NPs (Cu NPs), acid-treated fish scale biochar (ATFSBM), and copper/acid-treated fish scale biochar (Cu/FS NCs) are depicted for comparison in Fig. 2(a), showing several peaks that reflect the complex nature of *Punica granatum* due to the presence of many biomolecules. The bands near 3260 cm^{-1}

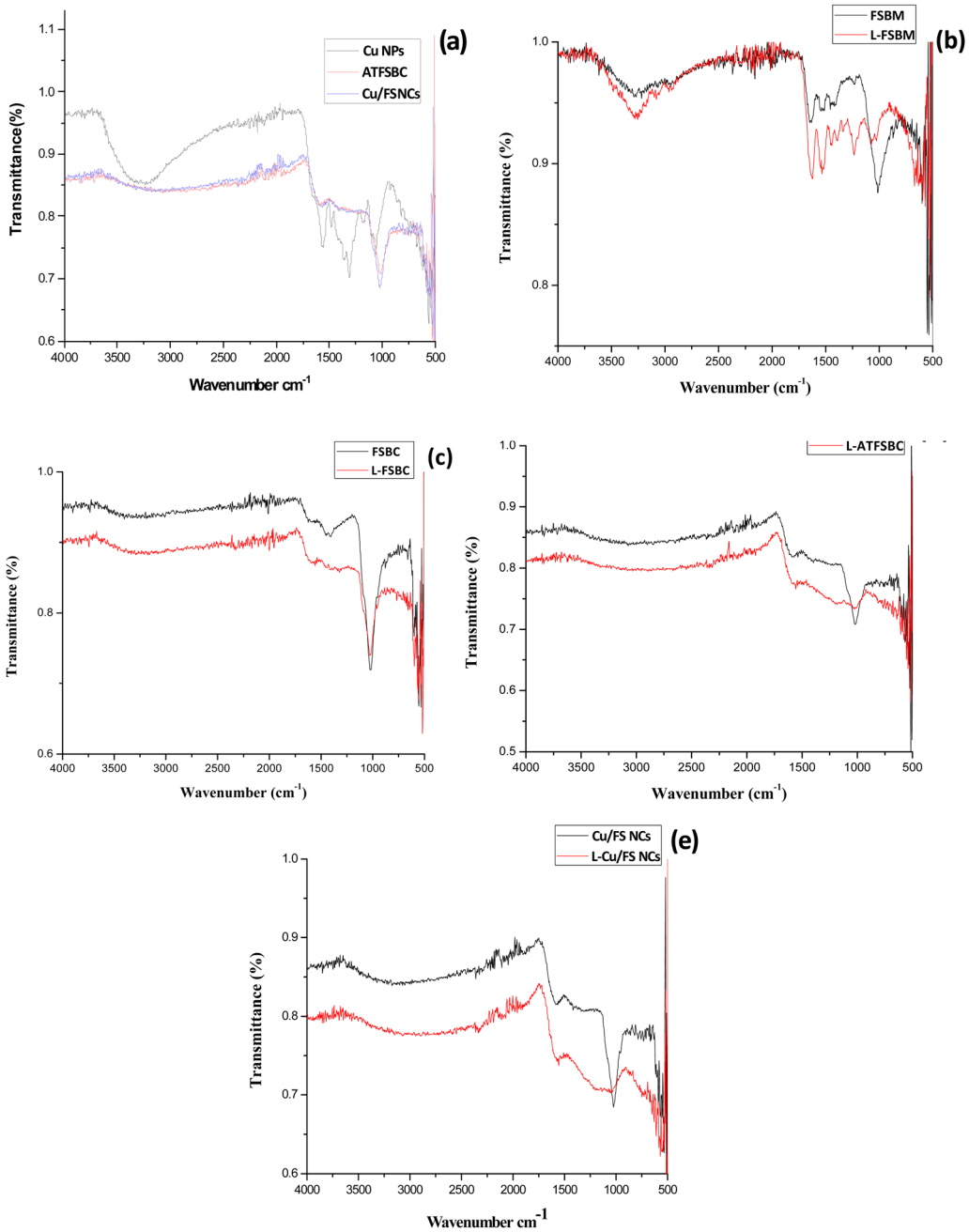

Fig. 2 (a) FTIR spectrum of CuNPs, ATFSBC, and Cu/FS NCs, (b) FSBM & loaded FSBM, (c) FSBC & loaded FSBC, (d) ATFSBC & loaded ATFSBC, and (e) Cu/FS NCs & loaded Cu/FS NCs.

Open Access Article. Published on 06 October 2025. Downloaded on 1/21/2026 7:21:53 AM.
This article is licensed under a Creative Commons Attribution 3.0 Unported Licence.

show aromatic and aliphatic C–H stretching, while multiple bands observed between 1956 and 2181 cm^{-1} are attributed to the stretching vibrations of C–OH and C═O of the protein that is responsible for the reducing, capping, and stabilizing process.[50] A clear disappearance of various bands can be seen when compared with that of the fish scale biomass. Fig. 2(d) presents the FTIR spectrum of acid-treated biochar (ATFSBC), the peaks of ATFSBC at 3661, 1936–2152, 1739, 1494, and 1015 cm^{-1} are indicative of O–H stretching, C–O stretching, C–C skeleton stretching, and phenyl groups, respectively. FTIR spectra of the green synthesized Cu/FS nanocomposites are presented in Fig. 2(e), and different peaks at 3677, 1965–2179, 1513, and 1023 cm^{-1} indicate functional groups of different phenolic compounds, the C═O stretching, C═C–C aromatic ring stretching, and C–O stretching.[51] FTIR analysis of Cu/FS NCs confirms that there was no variation in functional groups after the fabrication of Cu NPs on acid-treated fish scale biochar. These functional groups are absorbed at the surface of green-synthesized copper nanocatalysts, which act as capping and stabilizing agents and increase the synergic effect and catalytic activity of the nanocomposite. In Fig. 2(b)–(e), FTIR spectra of loaded DR 227 by adsorbents such as L-FSBM, L-FSBC, L-ATFSBC, and L-Cu/FS NCs were also represented in comparison with FSBM, FSBC, ATFSBC, and Cu/FS NCs. The change in the spectrum of adsorbents after adsorption of dye indicated the complexation of different compounds of the adsorbent with dye. Additionally, after the adsorption by FSBM, FSBC, ATFSBC, and Cu/FS NCs, peak elongation, peak broadening, and reduction in the intensity of peaks were seen, which demonstrated the dye-functional group interaction in the adsorption process.[52] It was seen in the FTIR spectrum that after the adsorption of dye, clear changes were seen in the loaded and unloaded adsorbents. Thus, it is concluded that bio-synthesized adsorbents are efficient and economical for the removal of anionic DR 227 dye.[42]

3.1.2. SEM/EDX analysis. Scanning electron microscopy can create an amplified image of a sample surface. An electron beam is used to produce a magnified image with a three-dimensional structure of the sample, which is used to study the pore size, shape, arrangement, and size of particles at the surface of the adsorbent. The morphology of Cu/FS NCs was observed before and after the adsorption phenomenon, as shown in Fig. 3(a–c). It is clear from SEM images that the pores at the surface of Cu/FS nanocomposites were assorted with inter-particle spaces and had nanoplates.[53] A large number of pores present at the surface of the original Cu/FS adsorbent provide an appropriate site for dyes to be adsorbed. SEM images obtained after the adsorption of DR 227 dye verified that the cavities and pores of Cu/FS adsorbent were proficiently crammed with adsorbate molecules in the form of flakes, as shown in Fig. 3(a–c). The pores at the surface of Cu/FS NCs were impregnated with molecules of dye, causing roughness of the surface and minimizing pore size.[54] It was determined that the size of the pores was decreased with the adsorption of the adsorbate dye molecules.[42] The EDX analysis of Cu/FS NCs is depicted in Fig. 3(d), and verified that Ca, C, O, P, Sb, and Cu are present as major

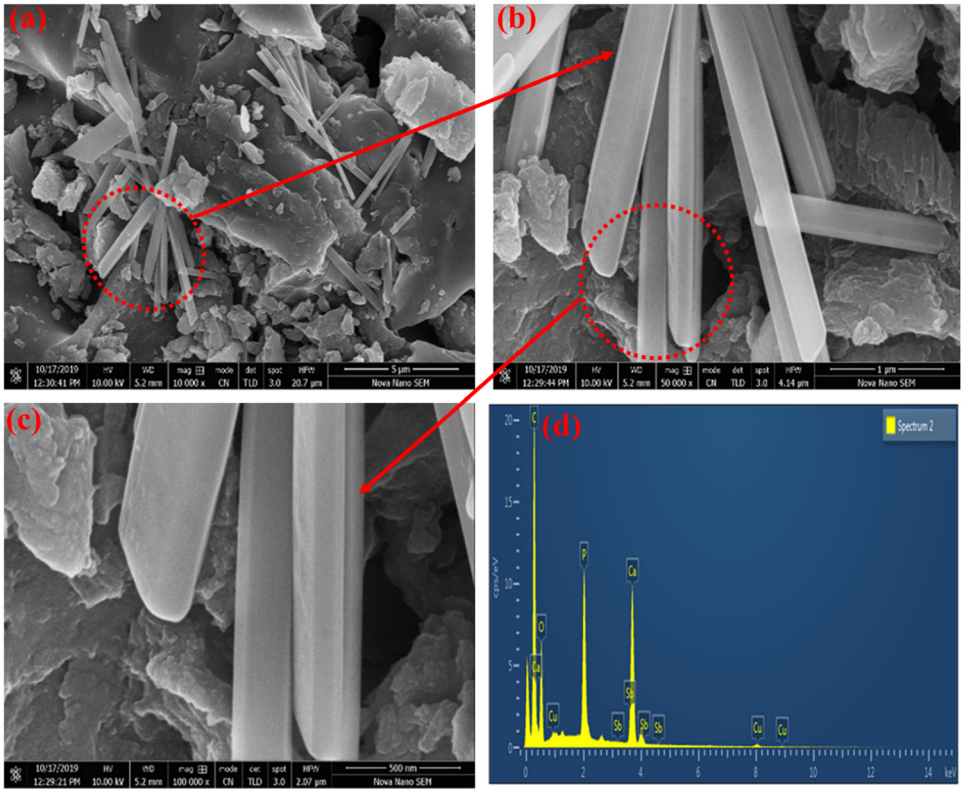

Fig. 3 (a)–(c) SEM of Cu/FS NCs and (d) EDX spectrum for Cu/FS NCs.

 © 2025 The Author(s). Published by the Royal Society of Chemistry

Open Access Article. Published on 06 October 2025. Downloaded on 1/21/2026 7:21:53 AM.
This article is licensed under a Creative Commons Attribution 3.0 Unported Licence.

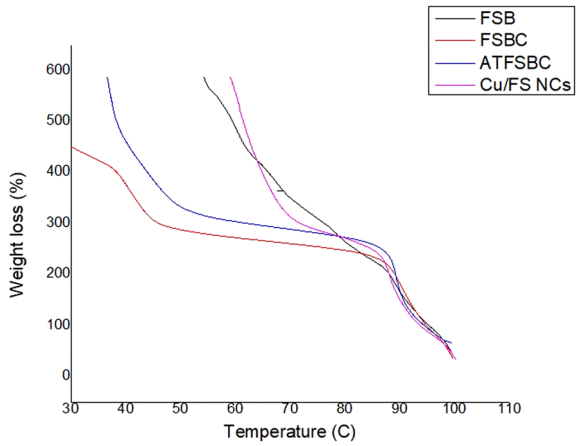

Fig. 4 TGA analysis at a temperature range of 100 °C to 600 °C.

components of Cu/FS adsorbent. These elements can develop ionic interactions with adsorbate molecules, which might affect the adsorption mechanism.[42,55]

3.1.3. Thermogravimetric analysis (TGA). Thermal analysis is a diagnostic technique used to evaluate the structural, chemical, and physical transformations that occur in a material because of temperature fluctuations. As a fundamental state variable, temperature profoundly influences various physical properties, structural changes, and chemical reactions. In this study, thermogravimetric analysis (TGA) was performed over a temperature range of 100 °C to 600 °C (Fig. 4). The results showed that the weight loss of FSBC and ATFSBC occurred consistently, ranging from 95% to 55%, as the temperature increased from 100 °C to 600 °C.[56] In contrast, FSBM and Cu/FS NC exhibited a sharp weight loss between 200 °C and 300 °C, followed by no further changes.

3.1.4. Point of zero charge. The properties of the absorbent determine the point of zero charge (pH_{pzc}), which is the pH at which the absorbent's surface charge is neutral. For synthesized composites, pH_{pzc} was measured *via* the solid addition method. The results are shown in Fig. 5(a). The results were 6, 6, 5, and 5 for FSBM, FSBC, ATFSBC, and Cu/FS NCs, respectively. The results indicate that sorbents develop a negative surface charge above pH_{pzc} and a positive charge below it, driven by the protonation of surface functional groups, enabling electrostatic interactions with dye anions.[57] Reactive dye adsorption is enhanced at pH_{pzc} due to the positive surface charge.[58]

3.1.5. Effect of pH. The effect of pH on the adsorption of DR 227 dyes was investigated by using FSBM, FSBC, ATFSBC, and Cu/FS NCs as adsorbents over a pH range of 1–10 while keeping the dosage of adsorbents (0.05 g), shaking speed (120 rpm), time (12 hours), and concentration (100 ppm) constant. In Fig. 5(b), it is shown that the adsorption of DR 227 by FSBM, FSBC, ATFSBC, and Cu/FS NCs was extremely affected by a change in pH. The maximum adsorption was seen at pH 2.0, after which a sharp decrease was observed with a further increase in pH.[59] The electrostatic force of attraction between adsorbent and adsorbate molecules was used to elucidate the effect of pH. Reactive dyes are chromophores based on azo groups, which release colored anions on dissociation. In an acidic environment, electrostatic forces of attraction facilitated the interaction between positively charged active sites on the adsorbent surface and negatively charged dye molecules, enhancing dye removal from the solution.[60] The percentage adsorption of adsorbate was significantly higher at low pH, suggesting protons' participation in the adsorption process. At pH 2, the surface functional groups of adsorbents undergo protonation, resulting in a positively charged surface that acts as a bridging ligand. This facilitates electrostatic interaction between the adsorbent and dye molecules, leading to enhanced adsorption. From pH 3–6, the adsorbent's surface charge becomes less positive due to decreased proton concentration, leading to reduced dye absorption. However, the further decrease in percentage adsorption from pH 6–10 predicted that there might be some other mechanism involved in the adsorption of dye other than electrostatic interactions, *i.e.*, hydrogen bonding and hydrophobic mechanisms. The maximum adsorption efficiency depicted in Fig. 5(b) for DR 227 was in the following order: 71% (FSBC) < 78% (FSBM) < 90% (ATFSBC) < 99.99% (Cu/FS NCs). It is graphically represented in Fig. 5(b) that the removal efficiency of biomass and biochar was lower compared to acid-treated biochar because the residual inorganic substances at the surface of native (biomass) and biochar will close the pores and make them non-porous and less efficient for adsorption of dyes.[46] The removal efficiency of synthesized Cu/FS NCs was greater than that of ATFSBC because ATFSBC acts as a solid support for Cu NPs, which helps to reduce the agglomeration of CuO NPs, enhances their stability, and facilitates their separation and recovery.[61,62] All experiments were performed in triplicate (n = 3) with a

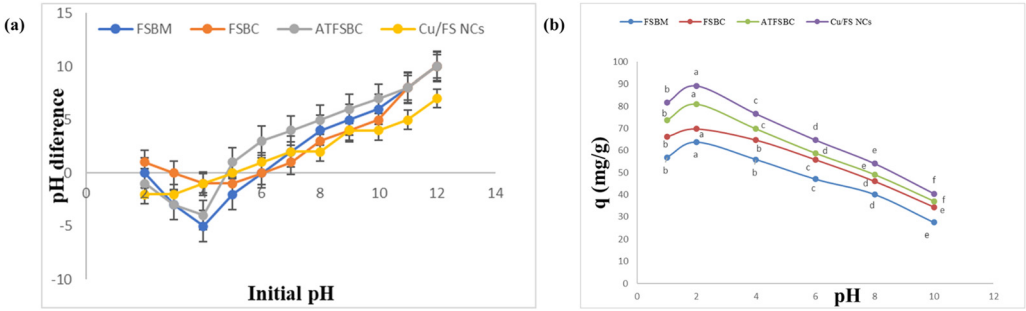

Fig. 5 (a) Point of zero charges, and (b) effect of pH.

Open Access Article. Published on 06 October 2025. Downloaded on 1/21/2026 7:21:53 AM.
This article is licensed under a Creative Commons Attribution 3.0 Unported Licence.

confidence interval of 0.05 and the values are given as standard deviation (S.D). One-way ANOVA was applied to data that had an F-ratio value of 361.75285 and R^2 of 0.99268, which suggests that there is a statistically significant difference between all the treatments ($P \leq 0.05$).

3.1.6. Proposed mechanisms of adsorption for pH. The suggested adsorption mechanism of DR 227 dye onto the produced adsorbents, particularly Cu/FS NCs and FSBC, transcends mere electrostatic interactions. At a low pH (pH = 2), the surface functional groups, including hydroxyl (–OH), carboxyl (–COOH), and amino (–NH_2), in fish scale-derived biochar become protonated, resulting in a positively charged surface that enhances the adsorption of anionic dyes such as DR 227 *via* electrostatic attraction. Nonetheless, the mechanism is not confined to this. Alongside the protonation of the adsorbent surface, the dye molecule may also experience protonation. The protonation of nitrogen-containing groups, such as pyridyl rings or azo linkages, can augment cationic interactions with the adsorbent surface, resulting in more robust electrostatic or donor–acceptor interactions than traditional π–π stacking alone. The energetically advantageous cation–π or cation–dipole interactions substantially enhance the binding affinity.

Furthermore, the partial carbonization of FSBC likely makes the material relatively hydrophobic due to the reduction of oxygenated polar groups. In this situation, hydrogen bonding synthons between the remaining hydroxyl or amine groups of collagen-derived peptides and sulfonic or azo groups on DR 227 may still occur, providing particular directed interactions. This substantiates the idea that hydrophobic effects and non-covalent interactions (*e.g.*, van der Waals forces, hydrogen bonding) function synergistically in dye retention.

The fish scale matrix comprises an intricate biochemical structure, predominantly consisting of collagen peptides, chitin/chitosan-like polysaccharides, and mineralized constituents such as calcium phosphate or carbonate. This varied composition presents an extensive array of functional groups carboxylic (–COOH), hydroxyl (–OH), amine (–NH_2), imine (–C═N), and carbonyl (C═O) capable of participating in diverse interactions such as coordination with Cu species, ion-exchange, complexation with azo or sulfonic groups of the dye, and hydrogen bonding. In the Cu/FS NCs system, the anchoring CuO NPs enhance the interaction processes by offering Lewis acidic sites for complexation and potentially facilitating redox interactions. The interaction between metal oxides and functionalized carbon surfaces improves adsorption through many mechanisms, such as chemisorption and surface complexation.[63,64]

$$\mathrm{ASOH} + \mathrm{H}^+ \rightarrow \mathrm{ASOH_2}^+ \quad (1)$$

$$\mathrm{Dye} + \mathrm{ASOH_2}^+ \rightarrow \mathrm{ASOH_2}^+\mathrm{Dye}^- \quad (2)$$

At basic pH,

$$\mathrm{ASOH} + \mathrm{OH}^- \rightarrow \mathrm{ASO}^- + \mathrm{H_2O} \quad (3)$$

$$\mathrm{ASO}^- + \mathrm{Dye}^- \rightarrow \mathrm{ASO}^-/\mathrm{Dye}^- \quad (4)$$

3.2. Effect of operational parameters

3.2.1. Effect of contact time. Optimizing contact time is vital for efficient and cost-effective large-scale treatment processes, necessitating a thorough investigation into its influence on Direct Acid 227 dye absorption. To explain the kinetic mechanism, absorbance was taken for DR 227 with different time intervals from 0–1440 while keeping pH (2), dosage of adsorbent (0.05 g), shaking speed (120 rpm), and concentration (100 ppm) constant. Fig. 6(a) shows the contact time on the adsorption of DR 227. The absorption kinetics displayed an initial rapid phase followed by a slower, equilibrium phase (360 min) for FSBM, FSBC, and ATFSBC, while Cu/FS NCs took about 240 min for 99.99% removal.[65] On further increasing contact, adsorption was not enhanced quickly; however, a minor change occurred. Within 120 min, FSBM, FSBC, ATFSBC, and Cu/FS NC adsorbents showed up to 70, 78, 85, and 92% removal for DR 227.[66] Initially, fast adsorption was seen because at the start of the experiment, many vacant active groups were present at the surface of the adsorbent. As time passed, the adsorption rate decreased until equilibrium was reached due to the saturation of active sites. Dye molecules undergo boundary attachment, surface interaction, and subsequent diffusion into the absorbent's permeable and porous structure, which requires a longer time. So, adsorption kinetics follow in two stages, the initial (rapid) and final (equilibrated) phase. The rapid adsorption may be due to the positive charge on the adsorbent's surface, which may interact with the anionic dye. As active sites became saturated, absorption was reduced due to the slow diffusion of adsorbent molecules from the boundary to the interior. Saeed *et al.* reported the use of the peel of *Trapa bispinosa's* for reactive orange 122, and parallel results were obtained from the study.[63] All experimental values are presented as mean ± SD from triplicate experiments. All experiments were performed in triplicate (n = 3), and the values are given as mean ± standard deviation (SD). One-way ANOVA was applied to data that showed an F-ratio value of 502.80732 and R^2 of 0.99472, which suggests that there is a statistically significant difference between all the treatments ($P \leq 0.05$).

3.2.2. Effect of dose. In the present research work, the optimum dose rate can be determined by using different amounts of catalysts that affect the adsorption efficiency of dyes. On average, an increase in absorbent concentration from 0.05 to 0.1 g resulted in a decrease in dye removal efficiency,[51] as shown in Fig. 6(b). It may be expected that with increasing the amount of adsorbent, the adsorbent–adsorbent interactions are stronger than adsorbate–adsorbent interactions. The absorbent dosage was optimized at 0.05 g, which was subsequently used in all experiments. Comparable results were obtained from similar studies, validating the findings.[67] The experiments were conducted in triplicate (n = 3), and the results are presented as the mean with the standard deviation (SD). There is a statistically significant difference in adsorption capacity when different treatments were applied, which predicts the mechanism of the adsorption process in the study.

3.2.3. Effect of concentration. The adsorbent's efficiency was elucidated through a systematic investigation of the

 © 2025 The Author(s). Published by the Royal Society of Chemistry

Open Access Article. Published on 06 October 2025. Downloaded on 1/21/2026 7:21:53 AM.
This article is licensed under a Creative Commons Attribution 3.0 Unported Licence.

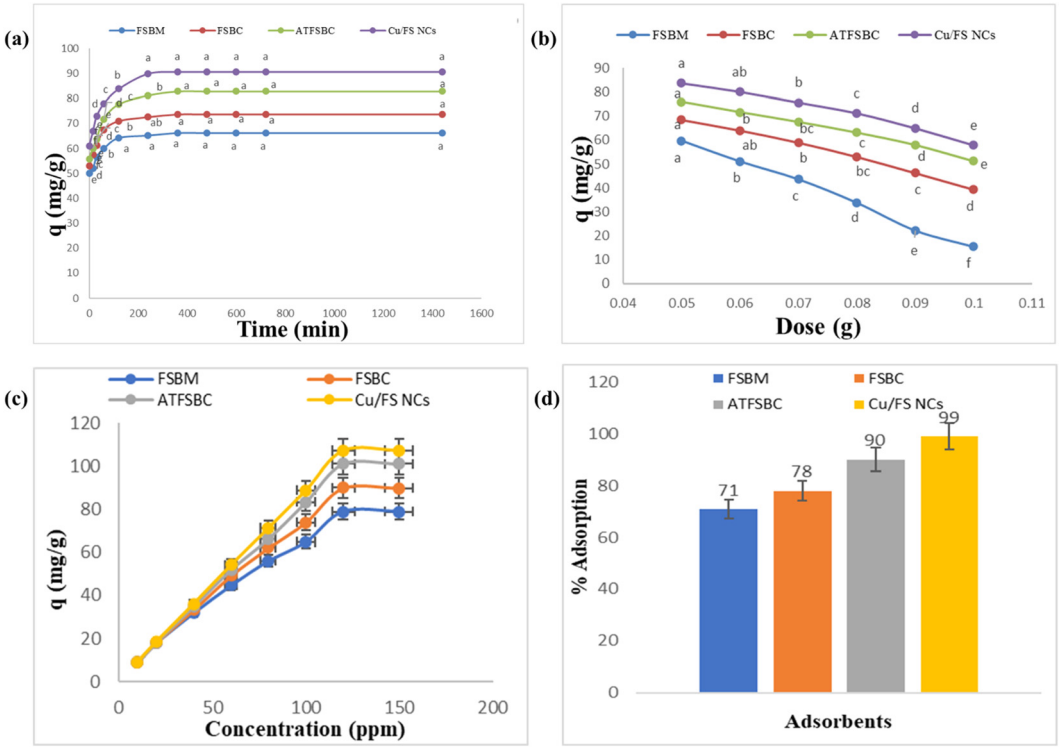

Fig. 6 Effect of operational parameters: (a) contact time, (b) catalyst dosage, (c) pollutant concentration, (d) the adsorption capabilities of FSBM compared to FSBC and ATFSBC compared to Cu/FS NCs exhibited no statistically significant differences at room temperature ($p > 0.05$), suggesting analogous performance under the present conditions.

percentage absorption *vs.* adsorbate initial concentration relationship. The impact of initial dye concentration on DR 227 by FSBM, FSBC, ATFSBC, and Cu/FS NC adsorbents (at pH: 2, initial concentrations (C_i: 10, 20, 50, 60, 100, 120, and 150 ppm), shaking speed: 120 rpm, adsorbent dose: 0.05 g, contact time: 12 hours) was studied. Fig. 6(c) shows the percentage adsorption *versus* dye initial concentration.[68] The collisions between anions of adsorbate and adsorbent are enhanced by increasing the dye's initial concentration up to 120 ppm, which enhances the adsorption process.[69] The absorption kinetics of DR 227 exhibited a positive correlation with initial concentration due to an increased ratio of active functional sites on the adsorbent's surface to the total adsorbate molecules in the dye's solution.[63] Contrary to this, a further increase from 120 ppm to 150 ppm in DR 227 dye concentrations causes a decrease in percentage adsorption because all the active binding sites may be occupied or saturated with dye molecules.[44] Similar behaviors were reported for RO 122 sorption by using the fruit and peel of *Trapa bispinosa* and the sorption of Reactive Yellow 160 on modified sand.[63,70]

3.2.4. Comparison among different adsorbents. In the present research work, adsorption of DR 227 was carried out by using different adsorbents such as FSBM, FSBC, ATFSBC, and Cu/FS NCs, and it was seen that the adsorption efficiency of Cu/FS nanocomposites is highest among all other adsorbents. At optimum conditions of pH, initial concentration of dyes, contact time, and adsorbent dosage rate, it was seen in Fig. 6(d) that the percentage adsorption of FSBM, FSBC, ATFSBC, and Cu/FS NCs for DR 227 was about 73%, 81%, 91%, and 99.99%, respectively.[71] Despite observable differences in the adsorption capabilities of the evaluated adsorbents, statistical analysis revealed that certain treatments had equivalent performance within the margin of experimental error ($\pm 3 \times$ SD). The adsorption capacity of FSBM was statistically comparable to that of FSBC, and similarly, ATFSBC exhibited no significant difference from Cu/FS NCs under the same conditions. These similarities indicate that, at normal temperature, the differentiation between these materials may not be distinctly evident. To more effectively differentiate the performance of various adsorbents, especially those exhibiting nuanced differences, it may be essential to conduct adsorption tests as a function of temperature to reveal thermally induced variations in behavior.

The enhanced adsorption efficacy of Cu/FS NCs relative to other adsorbents (FSBM, FSBC, ATFSBC) is predominantly due to the synergistic effect of CuO NPs affixed to the surface of acid-treated biochar. The inclusion of CuO NPs enhances surface heterogeneity and provides extra active adsorption sites, such as metal–oxygen functional groups capable of participating in surface complexation, cation–π interactions, and Lewis acid–base interactions with dye molecules. Moreover, CuO NPs exhibit a strong attraction for the functional groups found in anionic dyes such as DR 227, including sulfonic acid and azo groups. The Cu^{2+} sites can establish coordination bonds with electron-donating groups, hence augmenting chemisorption. This interaction possesses greater energy strength than mere physical adsorption and enhances the existing processes (electrostatic, hydrogen bonding) offered by the biochar matrix. Furthermore, the uniformly

Open Access Article. Published on 06 October 2025. Downloaded on 1/21/2026 7:21:53 AM.
This article is licensed under a Creative Commons Attribution 3.0 Unported Licence.

distributed Cu NPs inhibit agglomeration by being stabilized on the porous carbon surface of ATFSBC, thereby preserving a large surface area and ensuring their accessibility. SEM investigation verified the development of nanoplate-like structures, enhancing the exposed surface area and facilitating better accessibility to Cu active sites. The presence of Cu indirectly affects the surface charge characteristics and wettability of the adsorbent, potentially modifying dye–surface interactions. Consequently, the Cu NPs not only offer supplementary chemical binding sites but also improve the structural and electrical characteristics of the adsorbent.

4. Adsorbents' recyclability

For commercial-scale applications, stability, recycling, adsorption percentage, and reusability of the absorbent are crucial factors. After adsorption, the Cu/FS nanocomposite was recovered through centrifugation, washed with 0.01 M NaOH followed by distilled water, and oven-dried at 80 °C to facilitate subsequent reactions.[72] It was also seen in Fig. 7 that the activity of the nano-copper biochar composite remained unchanged after four cycles of separation, demonstrating its potential for reuse up to four times without loss of performance. Table 1 presents a comparative analysis of the adsorption of different pollutants.

5. Adsorption kinetic modeling

The adsorption kinetic model is vital for optimizing industrial processes, offering useful information regarding the rate of dye transfer and the absorbent's retention time. In this study, the adsorption kinetics of DR 227 dye were analyzed at various time intervals to characterize the behavior of FSBM, FSBC, ATFSBC, and Cu/FS NC adsorbents.

5.1. Pseudo-first order

The rate of reaction is proportional to vacant sites on the adsorbent surface.

$$\log(q_e - q_t) = \log q_e - \frac{K_1 t}{2.303}$$

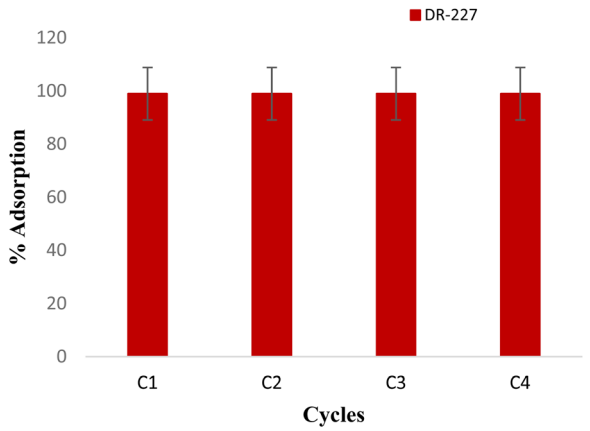

Fig. 7 Reusability performance of the catalyst across 4 consecutive cycles.

Table 1 A comparative analysis of the adsorption of different pollutants

Biomass	NPs	Pollutant	Amount of pollutant	Dose of adsorbent	Contact time	Degradation efficiency	Adsorption capacity	Ref.
Coconut biochar	CuO–NiO	CIP	50 mg	10 ppm	120	95.15%	880.3 mg g^{-1}	72
Fish scale	ZnO	Cr(vi)	100 mg	1.25 g L^{-1}	180	98.70%	48.08 and 90.09 mg g^{-1}	73
Fish scale	MgO	Cu^{2+}, Cd^{2+}, and Pb^{2}	100 mg L^{-1}	20 mg	180	84.2%, 74.2%, and 53.7%	505.8, 327.2, and 661.2 mg g^{-1}	74
Cladophora algae	CuO	TC	50 mg L^{-1}	15.60 mg g^{-1}) mg L^{-1}	240	96%	—	75
Phyllanthus emblica	CuO	Arsenic(v)	1 mg L^{-1}	2.5 g L^{-1}	400	85%	1152.5 μg g^{-1}	76
Rapa natans L. shells@ polyamide-12		Methyl orange & brilliant green	100 mg L^{-1}	0.1 g	240	93.90% & 97.30%	166.60 & 55.24 mg g^{-1}	77
Nyctanthesarbor-tristis.	CuO	U(vi), Pb(ii), Cr(vi), and Cd(ii)	100 mg L^{-1}	0.01 g	120	82.5%, 74%, 73.2, & 65.4	200, 155.27, 131.57 & 90.90 mg g^{-1}	78
Xanthan gum Xanthate-*graft*-poly(acrylic acid	CuO	MB	100 mg L^{-1}	1.2 g L^{-1}	—	90.2%	132.10 mg g^{-1}	79
Albizia saman	CuO	CR	—	1.1 mg g^{-1}	120 min	54%	17.53 mg g^{-1}	80
Fish scale	**Cu**	**DR 227 Dye**	**10–100 mg L^{-1}**	**0.05 g**	**240 min**	**99.99%**	**476.19 mg g^{-1}**	**This work**

 © 2025 The Author(s). Published by the Royal Society of Chemistry

Open Access Article. Published on 06 October 2025. Downloaded on 1/21/2026 7:21:53 AM.
This article is licensed under a Creative Commons Attribution 3.0 Unported Licence.

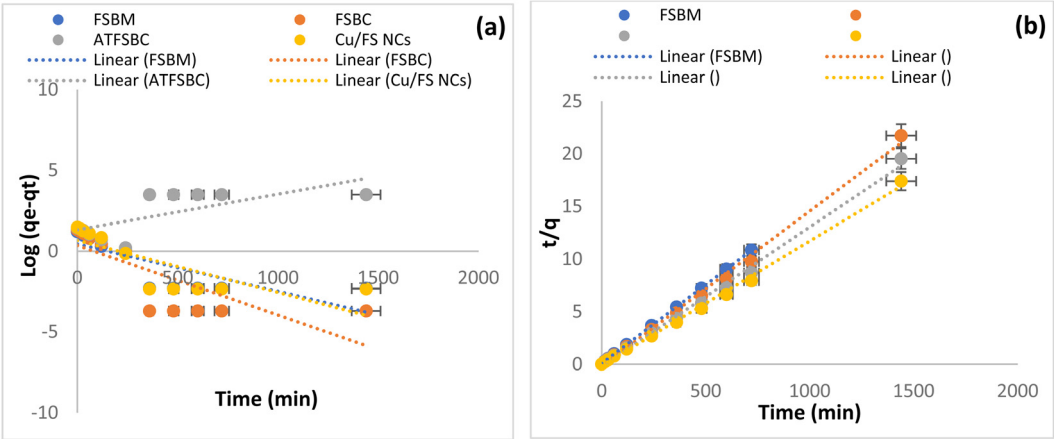

Fig. 8 (a) Adsorption kinetic models, pseudo-first order, (b) pseudo-second-order plots of DR 227 by FSBM, FSBC, ATFSBC, and Cu/FS NCs. The strong alignment with pseudo-second-order kinetics indicates that the adsorption process entails intricate and cooperative supramolecular interactions between the dye and the functional sites on the adsorbent.

where K_1 (per min), q_t (mg g^{-1}), and q_e (mg g^{-1}) are the adsorption rate constant, the amount of adsorption at a time "t", and the amount of adsorption of dye at equilibrium. In Fig. 8(a), the non-linear plot between $\log(q_e - q_t)$ *versus* t and low regression coefficient (R^2) value suggests that the pseudo-first-order kinetic model is inadequate for describing the adsorption mechanism of DR 227. A comparative analysis of pseudo-first-order and pseudo-second-order kinetic models revealed that the former was less suitable for describing the biosorption kinetics of RO 22 onto *Trapa bispinosa*.[63]

5.2. Pseudo-second order equation

In the pseudo-second-order kinetic model, the pseudo-second-order kinetic model assumes a proportional relationship between the adsorption rate and the square of the available sites on the adsorbent surface.

$$\frac{t}{q_t} = \frac{1}{K_2 q_e^2} + \frac{1}{q_e t}$$

K_2 (mg g^{-1} min^{-1}) is the adsorption rate constant for the pseudo-second-order reaction. In Fig. 8(b) the plots of t/q_t *versus* t exhibited a linear relationship with a high regression coefficient (R^2) value, indicating a strong correlation. As presented in Table 2, the kinetic parameters suggest that absorption is the rate-controlling step in the overall absorption process. The data analysis revealed a good fit between the theoretical and experimental q_e values for the pseudo-second-order model, indicating its suitability for describing the adsorption kinetics of DR 227 dye. The pseudo-second-order kinetic model exhibited an R^2 value approaching unity (1), confirming its suitability for describing the adsorption process. The findings collectively indicate that the pseudo-second-order kinetic model is the most accurate descriptor of DR 227 dye adsorption. The isotherm illustrates the distribution of molecules between the liquid and solid phases at equilibrium, and the results are consistent with the findings of this study.[63]

Both adsorbate concentration and adsorbent site availability play a crucial role in determining the adsorption rate. The adsorption mechanism may involve chemical adsorption (chemisorption), where the adsorbate forms chemical bonds with the adsorbent, requiring more energy and involving electron transfer. In short, the experimental data fit the pseudo-second-order (PSO) model, indicating a chemisorption mechanism where the adsorption rate depends on both adsorbate concentration and available adsorption sites.[81]

The excellent alignment of the experimental data with the pseudo-second-order kinetic model ($R^2 \approx 0.999$) suggests that the rate-limiting step is chemisorption, wherein the adsorption process is influenced by both the dye concentration and the accessibility of active binding sites on the adsorbent surface. This indicates the establishment of more robust, precise interactions –potentially encompassing supramolecular binding processes. Within the Cu/FS NCs adsorbent system, these interactions presumably result from a confluence of hydrogen

Table 2 Comparison between pseudo 1st order and pseudo 2nd order kinetic models for DR 227

		Pseudo 1st order			Pseudo 2nd order				IDP		
Adsorbate (dye)	Adsorbent (catalysts)	q_e (mg g^{-1})	K_{1ad} (min^{-1})	R^2	q_{exp} (mg g^{-1})	q_e (mg g^{-1})	K_{2ad} (g mg^{-1} min^{-1})	R^2	K_{pi}	C_i	R^2
RR-227	FSBM	0.706	−0.0038	0.6101	66.29	68.027	0.00289	0.9999	2.76	55.87	0.892
	FSBC	0.058	−0.0016	0.1324	73.74	66.225	0.00056	0.9945	4.32	35.76	0.912
	ATFSBC	8.496	−0.0004	0.5332	82.811	62.112	−0.0005	0.9826	3.77	42.12	0.732
	Cu/FS NCs	8.648	−0.0005	0.5047	90.63	84.034	0.00215	0.9999	2.99	32.88	0.932

Open Access Article. Published on 06 October 2025. Downloaded on 1/21/2026 7:21:53 AM.
This article is licensed under a Creative Commons Attribution 3.0 Unported Licence.

bonding, electrostatic attraction, π–π stacking, and metal–ligand complexation between the dye molecules and surface functional groups.[82] The self-completeness feature of pseudo-second-order kinetics indicates that the adsorption process continues until a specific equilibrium is attained, demonstrating a structured, cooperative interaction network akin to supramolecular host–guest systems. The multivalent functional groups in biochar (–OH, –COOH, $–NH_2$, *etc.*) and the coordination capabilities of Cu^{2+} sites facilitate such mechanisms. These facilitate both surface adsorption and molecular recognition-like behavior, hence augmenting selectivity and binding affinity for the dye molecules, by the principles of supramolecular chemistry.[83]

5.3. Intraparticle diffusion model

Biosorption of dye molecules from wastewater onto the biosorbent surface is a multi-phase process. The biosorption of dye molecules onto the biosorbent surface involves a three-stage intraparticle diffusion process.

Stage 1: Film or surface diffusion-sorbate molecules migrate from the bulk solution to the absorbent surface *via* molecular diffusion.

Stage 2: Intraparticle diffusion-sorbate molecules diffuse through the biosorbent's pore structure, reaching internal binding sites.

Stage 3: Adsorption-sorbate molecules interact with functional groups on the interior pore surfaces, forming chemical bonds and achieving thermodynamic equilibrium.

$$q_t = k_{pi}t^{1/2} + C_i$$

In this equation, C_i specifies the boundary layer thickness, whereas the k_{pi} (mg g^{-1} $min^{-1/2}$) denotes the rate constant of intraparticle diffusion. Their values can be calculated from the intercept and slope by plotting q_t against $t^{1/2}$, respectively.[84]

5.4. Adsorption equilibrium studies

Adsorption equilibrium models are employed to investigate the adsorption process, specifically the interactions between adsorbate and adsorbent at equilibrium, and to estimate the maximum adsorption capacity of the adsorbent. The biosorption isotherm is a graphical representation of the equilibrium relationship between the concentration of dye molecules in solution and the amount adsorbed onto the biosorbent. The sorption isotherm describes the relationship between the amount of sorbate sorbed per unit amount of sorbent and the remaining sorbate concentration in the solution at a constant temperature and under equilibrium conditions. To ensure the effective practical implementation of biosorption systems, a thorough understanding of biosorption isotherms is crucial, and this can be achieved by analyzing various established models, *i.e.*, Langmuir and Freundlich biosorption isotherms.

5.5. Langmuir isotherm

The Langmuir model accurately describes monolayer adsorption processes, which assumes that the adsorbent surface has a finite number of adsorption sites, which are energetically equivalent and can accommodate only one adsorbate molecule. The maximum adsorption capacity is attained when the adsorbent surface is fully saturated with a monolayer of adsorbate molecules, beyond which no further adsorption can occur. The presented equation enables the quantitative evaluation of the monolayer adsorption capacity (q_e mg g^{-1}), as well as other thermodynamic parameters that govern the adsorption process.

$$\frac{C_e}{q_e} = \frac{1}{X_m K_L} + \frac{C_e}{X_m}$$

where q_e (mg g^{-1}), C_e (mg L^{-1}), and X_m (mg g^{-1}) represent the equilibrium sorption capacity, the concentration of dye at equilibrium, and the complete monolayer or adsorption capacity, and K_L is the Langmuir constant. The low R^2 value obtained from the non-linear plot of C_e/q_e against C_e confirms that the adsorption of DR 227 does not conform to the Langmuir model, implying a more complex adsorption mechanism as shown in Fig. 9(a), and the results are supported by ref. 63.

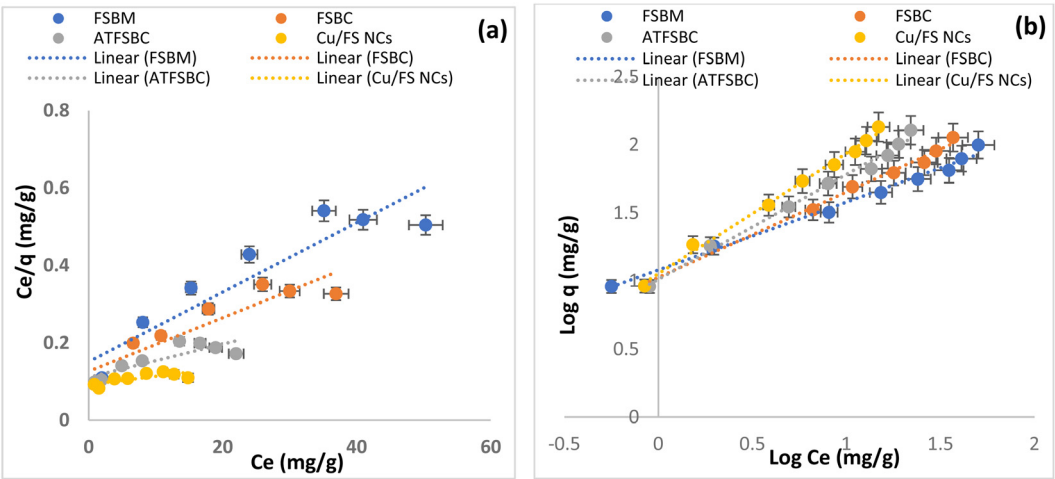

Fig. 9 (a) Adsorption equilibrium models, Langmuir and (b) Freundlich models of adsorption of DR 227 by FSBM, FSBC, ATFSBC, and Cu/FS NCs.

 © 2025 The Author(s). Published by the Royal Society of Chemistry

Open Access Article. Published on 06 October 2025. Downloaded on 1/21/2026 7:21:53 AM.
This article is licensed under a Creative Commons Attribution 3.0 Unported Licence.

Table 3 Equilibrium isotherm parameters for Reactive Red 227

Adsorbate (dye)	Adsorbent (catalysts)	Langmuir model			Exp value	Freundlich model			
		X_m (mg g^{-1})	K_L (L mg^{-1})	R^2	q_{exp} (mg g^{-1})	q_e (mg g^{-1})	$1/n$	K_F (mg g^{-1})	R^2
RR 227	FSBM	111.12	0.060	0.8671	66.29	71.19	0.499	0.077	0.9895
	FSBC	144.93	0.055	0.8608	73.74	82.14	0.628	0.025	0.9899
	ATFSBC	232.56	0.039	0.7174	83.81	89.67	0.771	0.012	0.9907
	Cu/FS NCs	476.19	0.023	0.5864	90.63	114.81	0.883	0.052	0.9939

Adsorbate (dye)	Adsorbent (catalysts)	Temkin				Harkins–Jura			
		q_m (mg g^{-1})	A	R^2	B	q_m (mg g^{-1})	A	B	R^2
RR 227	FSBM	4.55	60.43	0.8671	10.11	7.4	75.34	2.26	0.9895
	FSBC	5.21	126.43	0.8608	15.43	14.21	126.5	1.79	0.9899
	ATFSBC	2.76	241.34	0.7174	21.56	19.45	712.2	3.75	0.9907
	Cu/FS NCs	6.29	93.24	0.5864	21.78	17.43	99.23	4.25	0.9939

5.6. Freundlich isotherm

The Freundlich model assumes multilayer adsorption, with adsorption capacity dependent on concentration. The model is mathematically expressed as:

$$\log q_e = \log K_f + \frac{1}{n \log C_e}$$

where the K_f (mg g^{-1}) and $1/n$ indicate adsorption capacity and adsorption intensity, respectively.

The Freundlich model was successfully applied to describe the adsorption of DR 227, with the Freundlich constants K_f and $1/n$ obtained from the plot of $\log q_e$ against $\log C_e$ as shown in Fig. 9(b) and Table 3. The value of $1/n$ less than one suggested a simple and efficient separation of dye from the solution. Moreover, the model recommended that adsorption occurred in multiple layers for DR 227, predicting a large number of active sites. The results indicated that the Freundlich model provided a better fit for DR 227 dyes as compared to the Langmuir model.[63]

5.7. Temkin biosorption isotherm

The Temkin biosorption isotherm relies on two fundamental assumptions. The first assumption posits that the heat of biosorption decreases linearly with surface coverage, driven by sorbate–biosorbent interactions. The second assumption asserts that the binding energies are uniformly distributed across the biosorbent surface (Temkin and Pyzhev, 1940). The Temkin biosorption isotherm is mathematically represented in linear form as:

$$q_e = B \ln A + B \ln C_e$$

In the Temkin biosorption isotherm equation, A and B are two essential constants. A denotes the Temkin equilibrium binding constant (L mg^{-1}), while B is a constant associated with the biosorption heat (J mole^{-1}). The expression for B is given as $B = RT/b$, where R is the universal gas constant (8.314 J mol^{-1} K^{-1}), T represents the absolute temperature (K), and b is the Temkin biosorption isotherm constant. By plotting q_e against $\ln C_e$, the values of A and B can be calculated from the intercept and slope, respectively.

5.8. Harkins–Jura biosorption isotherm

The Harkins–Jura biosorption isotherm describes a biosorption process characterized by the formation of multilayers of sorbate molecules on the biosorbent surface, resulting from the heterogeneous distribution of pores (Harkins and Jura, 1944).[85] The linearized expression for this model is given by

$$\frac{1}{q_e^2} = \frac{B}{A} - \frac{1}{A} \log C_e$$

here, A is the Harkins–Jura isotherm parameter, and B is the corresponding isotherm constant.

6. Conclusion

The findings of this research demonstrate that biosynthesized nano Cu-biochar composites might work as active agents for the adsorption of different textile azo dyes. For DR 227, the optimal conditions for maximum adsorption capacity of all adsorbents (FSBM, FSBC, ATFSBC, and Cu/FS NCs) were identified at pH 2, with an initial concentration of 120 ppm, contact time (360 min for DR 227 by using FSBM, FSBC, and ATFSBC, while Cu/FS NCs take about 240 min), and adsorbent dosage rate (0.05 g). The stability of nano Cu-biochar composites was investigated by desorption reactions and demonstrated stable adsorption performance over four consecutives cycles. The thermodynamic study revealed that the process was thermodynamically favored, releasing heat (exothermic) and exhibiting increased entropy with elevated temperatures. Experimental data on the adsorption process were analyzed using several isotherm and kinetic models, the findings revealed that the pseudo-second-order (R^2 = 0.999) and the Freundlich isotherm (R^2 = 0.9939) provided the best correlation with the experimental data. From the results, it is evident that the biosynthesized nano Cu-biochar composite exhibits significantly higher efficiency compared to the other biomass, biochar, and acid-treated biochar, indicating its potential as a highly effective adsorbent for removing various textile dyes from wastewater, making it a valuable material for future environmental applications.

Open Access Article. Published on 06 October 2025. Downloaded on 1/21/2026 7:21:53 AM.
This article is licensed under a Creative Commons Attribution 3.0 Unported Licence.

Conflicts of interest

There are no conflicts to declare.

Data availability

The data that support the plots in this paper and other findings of this study are available from the corresponding author upon reasonable request.

References

1 J. A. Malvestiti, *et al.*, Comparative study of the efficiency of conventional and green-prepared iron nanoparticles for catalytic ozonation, *Catal. Today*, 2024, **430**, 114521.
2 M. Pipíška, *et al.*, Removal of Synthetic Dyes by Dried Biomass of Freshwater Moss Vesicularia Dubyana: A Batch Biosorption Study, *Environments*, 2018, **5**(1), 10.
3 L. Meili, *et al.*, Adsorption of methylene blue on agroindustrial wastes: Experimental investigation and phenomenological modelling, *Prog. Biophys. Mol. Biol.*, 2018, **141**, 60–71.
4 M. Ismail, *et al.*, Green synthesis of plant supported CuAg and CuNi bimetallic nanoparticles in the reduction of nitrophenols and organic dyes for water treatment, *J. Mol. Liq.*, 2018, **260**, 78–91.
5 W. L. da Silva, M. A. Lansarin and J. H. dos Santos, Industrial and agroindustrial wastes: an echotechnological approach to the production of supported photocatalysts, *Water Sci. Technol.*, 2016, **73**(1), 28–38.
6 S. Mishra and A. Maiti, The efficacy of bacterial species to decolourise reactive azo, anthroquinone and triphenylmethane dyes from wastewater: a review, *Environ. Sci. Pollut. Res.*, 2018, 1–29.
7 M. Nasrollahzadeh, Z. Issaabadi and S. M. Sajadi, Green synthesis of a Cu/MgO nanocomposite by Cassytha filiformis L. extract and investigation of its catalytic activity in the reduction of methylene blue, congo red and nitro compounds in aqueous media, *RSC Adv.*, 2018, **8**(7), 3723–3735.
8 M. N. Subramaniam, *et al.*, Photocatalytic membranes: a new perspective for persistent organic pollutants removal, *Environ. Sci. Pollut. Res.*, 2022, **29**(9), 12506–12530.
9 F. Batool, *et al.*, Biosynthesis of copper nanoparticles using Bacillus flexus and estimation of their potential for decolorization of azo dyes and textile wastewater treatment, *J. King Saud Univ., Sci.*, 2024, 103309.
10 A. C. Del Álamo, *et al.*, Trametes versicolor immobilized on rotating biological contactors as alternative biological treatment for the removal of emerging concern micropollutants, *Water Res.*, 2020, **170**, 115313.
11 S. Rajendrachari, *et al.*, Electrochemical oxidation of methylene blue dye in wastewater using mechanically alloyed high entropy alloy modified carbon paste electrode using cyclic voltammetry, *Mater. Res. Express*, 2023, **10**(5), 054003.
12 R. Pelalak, R. Alizadeh and E. Ghareshabani, Enhanced heterogeneous catalytic ozonation of pharmaceutical pollutants using a novel nanostructure of iron-based mineral prepared via plasma technology: A comparative study, *J. Hazard. Mater.*, 2020, **392**, 122269.
13 E. S. Al-Farraj, *et al.*, Efficient Photocatalytic Decomposition of Acid Blue 25 Dye using Facilely Synthesized Magnesium Aluminate Nanoparticles, *Water Conserv. Sci. Eng.*, 2024, **9**(1), 3.
14 D. Awfa, *et al.*, Photocatalytic degradation of organic micropollutants: Inhibition mechanisms by different fractions of natural organic matter, *Water Res.*, 2020, **174**, 115643.
15 W. L. da Silva and J. H. dos Santos, Ecotechnological strategies in the development of alternative photocatalysts, *Curr. Opin. Green Sustainable Chem.*, 2017, **6**, 63–68.
16 S. N. H. Azmi, *et al.*, Development of a citric-acid-modified cellulose adsorbent derived from Moringa peregrina leaf for adsorptive removal of citalopram HBr in aqueous solutions, *Pharmaceuticals*, 2022, **15**(6), 760.
17 K. Nain, *et al.*, Adsorption potential of ionic liquid-modified ZnO nanoparticles for highly efficient removal of azo dye: detailed isotherms and kinetics, *Environ. Sci. Pollut. Res.*, 2024, **31**(28), 40083–40099.
18 N. Rahman and P. Varshney, Assessment of ampicillin removal efficiency from aqueous solution by polydopamine/zirconium (IV) iodate: optimization by response surface methodology, *RSC Adv.*, 2020, **10**(34), 20322–20337.
19 L. M. Alshandoudi, *et al.*, Synthesis and characterization of nano zinc oxide/zinc chloride–activated carbon composite based on date palm fronds: adsorption of methylene blue, *Biomass Convers. Biorefin.*, 2024, **14**(15), 17219–17233.
20 M. K. Okla, *et al.*, Environmental friendly nano-star CdS coupled ZnS on bi-polymer matrix: Unravelling defects-rich nanoplatform for ultrahigh white light active direct S-scheme photodegradation of organic pollutants, *J. Alloys Compd.*, 2022, **925**, 166611.
21 H. Ouallal, *et al.*, Study of acid treatment effect of a natural red clay onto physico-chemical and adsorption properties, *Desalin. Water Treat.*, 2023, **315**, 96–110.
22 M. Radenković, *et al.*, Waste biomass derived highly-porous carbon material for toxic metal removal: Optimisation, mechanisms and environmental implications, *Chemosphere*, 2024, **347**, 140684.
23 P. Kumar, Biochar Production from Marine Algae and Its Application in the Treatment of Industrial Effluent. *Marine Biomass: Biorefinery, Bioproducts and Environmental Bioremediation*, 2024: 57.
24 M. A. Salem, *et al.*, Adsorptive dye removal by Cu (II)-modified silica-alumina/polyaniline nanocomposite, *Mater. Chem. Phys.*, 2024, **325**, 129795.
25 N. W. Akpanudo, *et al.*, Application of Activated Carbon Prepared from Nypa Palm Seed Husk in the Adsorption of Azo Dyes from Waste Water and Evaluation of the Adsorption Isotherms, *J. Mater. Sci. Res. Rev.*, 2024, **7**(2), 210–217.
26 S. J. Anwar, *et al.*, Remediation of Dye-Contaminated Water Using Brown Algae Seaweed Supported Copper Nanoparticles, *Arabian J. Sci. Eng.*, 2024, **49**(1), 475–496.
27 N. W. Akpanudo and O. M. Olabemiwo, Green synthesis and characterization of copper nanoparticles (CuNPs) and

 © 2025 The Author(s). Published by the Royal Society of Chemistry

Open Access Article. Published on 06 October 2025. Downloaded on 1/21/2026 7:21:53 AM.
This article is licensed under a Creative Commons Attribution 3.0 Unported Licence.

composites (CuC) using the Echinochloa pyramidalis extract and their application in the remediation of PAHsin water, *Water Pract. Technol.*, 2024, **19**(2), 324–342.

28 M. A.-I. Imon, *et al.*, Evaluation of anthelmintic and antioxidant efficacy of green-synthesized copper nanoparticles derived from Erioglossum rubiginosum leaf and seed aqueous extracts, *Eur. J. Med. Chem. Rep.*, 2024, **12**, 100181.

29 P. Muraro, *et al.*, Ecotoxicity and in vitro safety profile of the eco-friendly silver and titanium dioxide nanoparticles, *Process Saf. Environ. Prot.*, 2024, **188**, 584–594.

30 L. F. W. Brum, *et al.*, Green synthesis of niobium (V) oxide nanoparticles using pecan nutshell (Carya illinoinensis) and evaluation of its antioxidant activity, *Catal. Today*, 2025, **445**, 115106.

31 L. B. de Menezes, *et al.*, In vitro safety profile and phyto-ecotoxicity assessment of the eco-friendly calcium oxide nanoparticles, *Chemosphere*, 2024, **365**, 143407.

32 L. D. Pompeu, *et al.*, Evaluation of cytotoxicity, reactive oxygen species and nitrous oxide of nanochitosan from shrimp shell, *Int. J. Biol. Macromol.*, 2023, **235**, 123730.

33 M. Nasrollahzadeh, Z. Issaabadi and S. M. Sajadi, Green synthesis of Cu/Al_2O_3 nanoparticles as efficient and recyclable catalyst for reduction of 2, 4-dinitrophenylhydrazine, Methylene blue and Congo red, *Composites, Part B*, 2019, **166**, 112–119.

34 A. Taghizadeh and K. Rad-Moghadam, Green fabrication of Cu/pistachio shell nanocomposite using Pistacia Vera L. hull: An efficient catalyst for expedient reduction of 4-nitrophenol and organic dyes, *J. Cleaner Prod.*, 2018, **198**, 1105–1119.

35 A. S. Shaban, *et al.*, Punica granatum peel extract mediated green synthesis of zinc oxide nanoparticles: structure and evaluation of their biological applications, *Biomass Convers. Biorefin.*, 2024, **14**(11), 12265–12281.

36 S. Abid, *et al.*, Synthesis of Metal Oxide Nanoparticles Using Punica granatum Extract for the Removal of Cationic and Anionic Dyes from Wastewater, *Arabian J. Sci. Eng.*, 2024, **49**(1), 515–530.

37 J. Singh, *et al.*, Pomegranate peel phytochemistry, pharmacological properties, methods of extraction, and its application: A comprehensive review, *ACS Omega*, 2023, **8**(39), 35452–35469.

38 R. Ghibate, *et al.*, Eco-friendly adsorption of Rhodamine B dye using Punica granatum peel from an aqueous medium. Green, *Anal. Chem.*, 2025, **12**, 100201.

39 S. S. A. M. K. Abad, *et al.*, Green synthesis of Pd@ biochar using the extract and biochar of corn-husk wastes for electrochemical Cr (VI) reduction in plating wastewater, *J. Environ. Chem. Eng.*, 2023, **11**(3), 109911.

40 X. Chen, *et al.*, Algal Biochar-Metal Nanocomposite Particles Tailor the Hydration Kinetics and Compressive Strength of Portland Cement Paste, *ACS Sustainable Chem. Eng.*, 2024, **12**(9), 3585–3594.

41 L. Pompeu, *et al.*, Adsorption of Rhodamine b dye onto novel Biochar: Isotherm, Kinetic, thermodynamic study and anti-biofilm activity, *Inorg. Chem. Commun.*, 2023, **158**, 111509.

42 S. M. Sajadi, *et al.*, Green synthesis of highly recyclable CuO/eggshell nanocomposite to efficient removal of aromatic containing compounds and reduction of 4-nitrophenol at room temperature, *Surf. Interfaces*, 2018, **13**, 205–215.

43 A. M. Aljeboree, *et al.*, Environmental removal of brilliant yellow dye onto porous adsorbent derived from pomegranate peels waste, *IOP Conf. Ser.: Earth Environ. Sci.*, 2022, **1029**, 012007.

44 J. Ooi, *et al.*, Assessment of fish scales waste as a low cost and eco-friendly adsorbent for removal of an azo dye: Equilibrium, kinetic and thermodynamic studies, *Bioresour. Technol.*, 2017, **245**, 656–664.

45 R. Nadeem, T. M. Ansari and A. M. Khalid, Fourier Transform Infrared Spectroscopic characterization and optimization of Pb (II) biosorption by fish (Labeo rohita) scales, *J. Hazard. Mater.*, 2008, **156**(1–3), 64–73.

46 F. Marrakchi, *et al.*, Mesoporous carbonaceous material from fish scales as low-cost adsorbent for reactive orange 16 adsorption, *J. Taiwan Inst. Chem. Eng.*, 2017, **71**, 47–54.

47 G. O. Achieng, *et al.*, Preparation, characterization of fish scales biochar and their applications in the removal of anionic indigo carmine dye from aqueous solutions, *Water Sci. Technol.*, 2019, **80**(11), 2218–2231.

48 M. Noman, *et al.*, Use of biogenic copper nanoparticles synthesized from a native Escherichia sp. as photocatalysts for azo dye degradation and treatment of textile effluents, *Environ. Pollut.*, 2020, **257**, 113514.

49 M. B. Mobarak, *et al.*, Synthesis and characterization of CuO nanoparticles utilizing waste fish scale and exploitation of XRD peak profile analysis for approximating the structural parameters, *Arabian J. Chem.*, 2022, **15**(10), 104117.

50 F. Ullah, *et al.*, Synergistic degradation of toxic azo dyes using Mn-CuO@ Biochar: An efficient adsorptive and photocatalytic approach for wastewater treatment, *Chem. Eng. Sci.*, 2025, **302**, 120844.

51 J. Iqbal, *et al.*, Nano-zerovalent manganese/biochar composite for the adsorptive and oxidative removal of Congo-red dye from aqueous solutions, *J. Hazard. Mater.*, 2021, **403**, 123854.

52 A. V. Selestin, *et al.*, Detailed analysis of crystal structure and optical properties of green synthesized nanoparticles: Application for photocatalyst degradation of methylene blue, *Trends Sci.*, 2022, **19**(24), 4430.

53 V. D. Mote, *et al.*, Structural, optical and magnetic properties of Mn-doped CuO nanoparticles by coprecipitation method, *Mater. Sci. Eng. B*, 2023, **289**, 116254.

54 S. Mansoori, *et al.*, CuOx-MnOy@ biochar nanocatalyst synthesis for heterogeneous visible-light-driven Fenton-like: a resistant antibiotic degradation, *Catal. Commun.*, 2022, **171**, 106517.

55 S. Khasim, *et al.*, Green synthesis of multifunctional Cu/MnO@ Biochar 3D structure as a high-performance anode material in Li-ion batteries and oxidative removal of Cango-red dye, *Case Stud. Chem. Environ. Eng.*, 2024, **9**, 100561.

56 R. R. Nair, M. M. Mondal and D. Weichgrebe, Biochar from co-pyrolysis of urban organic wastes—investigation of

Open Access Article. Published on 06 October 2025. Downloaded on 1/21/2026 7:21:53 AM.
This article is licensed under a Creative Commons Attribution 3.0 Unported Licence.

carbon sink potential using ATR-FTIR and TGA, *Biomass Convers. Biorefin.*, 2022, **12**(10), 4729–4743.

57 M. Bellaj, *et al.*, Cationic and anionic dyes adsorption from wastewater by clay-chitosan composite: an integrated experimental and modeling study, *Chem. Eng. Sci.*, 2024, **285**, 119615.

58 N. Rahman, *et al.*, Fractal-like kinetic modelling for sorption of diclofenac onto graphene oxide/polypyrrole composite: Mechanism analysis and response surface methodology for optimization, *Diamond Relat. Mater.*, 2023, **139**, 110328.

59 J. Chen, *et al.*, Removal of multiple heavy metals from mining-impacted water by biochar-filled constructed wetlands: adsorption and biotic removal routes, *Bioresour. Technol.*, 2021, **331**, 125061.

60 D. Li, *et al.*, Use of multiple water surface flow constructed wetlands for non-point source water pollution control, *Appl. Microbiol. Biotechnol.*, 2018, **102**, 5355–5368.

61 A. Rostami-Vartooni, M. Nasrollahzadeh and M. Alizadeh, Green synthesis of seashell supported silver nanoparticles using Bunium persicum seeds extract: application of the particles for catalytic reduction of organic dyes, *J. Colloid Interface Sci.*, 2016, **470**, 268–275.

62 M. Nasrollahzadeh, M. Atarod and S. M. Sajadi, Green synthesis of the Cu/Fe_3O_4 nanoparticles using Morinda morindoides leaf aqueous extract: a highly efficient magnetically separable catalyst for the reduction of organic dyes in aqueous medium at room temperature, *Appl. Surf. Sci.*, 2016, **364**, 636–644.

63 M. Saeed, R. Nadeem and M. Yousaf, Removal of industrial pollutant (Reactive Orange 122 dye) using environment-friendly sorbent Trapa bispinosa's peel and fruit, *Int. J. Environ. Sci. Technol.*, 2015, **12**(4), 1223–1234.

64 J. Arévalo-Fester and A. Briceño, Insights into selective removal by dye adsorption on hydrophobic vs multivalent hydrophilic functionalized MWCNTs, *ACS Omega*, 2023, **8**(12), 11233–11250.

65 A. J. Gogoi and A. K. Pulikkal, Propane-1, 3-bis (hexadecyl-dimethylammonium bromide)-bentonite-based novel hybrid material for the elimination of textile dyes, *J. Mol. Liq.*, 2024, **395**, 123890.

66 S. Varshney and A. Gupta, Forest industrial biomass residue-mediated green synthesized multifunctional copper oxide nanoparticles for efficient wastewater treatment and biomedical applications, *J. Cleaner Prod.*, 2024, **434**, 140109.

67 R. Nadeem, *et al.*, Pb (II) sorption by pyrolysed Pongamia pinnata pods carbon (PPPC), *Chem. Eng. J.*, 2009, **152**(1), 54–63.

68 S. Anvari, *et al.*, Design of chitosan/boehmite biocomposite for the removal of anionic and nonionic dyes from aqueous solutions: adsorption isotherms, kinetics, and thermodynamics studies, *Int. J. Biol. Macromol.*, 2024, **259**, 129219.

69 A. R. Binupriya, *et al.*, Sequestration of Reactive Blue 4 by free and immobilized Bacillus subtilis cells and its extracellular polysaccharides, *Colloids Surf., B*, 2010, **76**(1), 179–185.

70 H. El Fargani, *et al.*, Removal of Reactive Yellow 160 from Industrial Wastewater onto Modified Sand (Sand of Larache city beach. Morocco), *Chem. Process Eng. Res.*, 2017, **52**, 24–36.

71 E. Rápó and S. Tonk, Factors affecting synthetic dye adsorption; desorption studies: a review of results from the last five years (2017–2021), *Molecules*, 2021, **26**(17), 5419.

72 R. Kumar, *et al.*, Biomass-Derived Biochar and CuO–NiO Nanocomposites: Eco-Friendly Solutions for Environmental Cleanup, *Int. J. Environ. Res.*, 2025, **19**(1), 1–22.

73 A. U. Islam, *et al.*, Potential of fish scale biochar nanocomposite with ZnO for effective sequestration of Cr (VI) from water: modeling and kinetics, *Int. J. Environ. Res.*, 2022, **16**(4), 51.

74 X. Qi, *et al.*, MgO-loaded nitrogen and phosphorus self-doped biochar: High-efficient adsorption of aquatic Cu^{2+}, Cd^{2+}, and Pb^{2+} and its remediation efficiency on heavy metal contaminated soil, *Chemosphere*, 2022, **294**, 133733.

75 M. S. Salman, *et al.*, Cladophora algae modified with CuO nanoparticles for tetracycline removal from aqueous solutions, *Water, Air, Soil Pollut.*, 2022, **233**(8), 321.

76 S. Saif, *et al.*, Adsorption studies of arsenic (V) by CuO nanoparticles synthesized by phyllanthus emblica leaf-extract-fueled solution combustion synthesis, *Sustainability*, 2021, **13**(4), 2017.

77 S. A. Aldahash, S. Siddiqui and M. K. Uddin, Eco-friendly synthesis of copper nanoparticles from fiber of Trapa natans L. shells and their impregnation onto polyamide-12 for environmental applications, *J. Nat. Fibers*, 2023, **20**(2), 2224976.

78 K. Kashyap, *et al.*, Adsorptive removal of heavy metal ions from aqueous solution by using green synthesized copper oxide nanoparticles, *Inorg. Nano-Met. Chem.*, 2025, **55**(5), 493–504.

79 K. Kashaudhan, *et al.*, Design of XGX-g-PAAHs@ CuO nanocomposite for efficient removal of methylene blue from water, *Sep. Sci. Technol.*, 2025, **60**(11), 1350–1369.

80 N. Choudhary, *et al.*, Phytonanofabrication of copper oxide from albizia saman and its potential as an antimicrobial agent and remediation of Congo red dye from wastewater, *Water*, 2023, **15**(21), 3787.

81 A. Raheem, N. Rahman and S. Khan, Monolayer Adsorption of Ciprofloxacin on Magnetic Inulin/Mg–Zn–Al Layered Double Hydroxide: Advanced Interpretation of the Adsorption Process, *Langmuir*, 2024, **40**(25), 12939–12953.

82 M. Abbas, *et al.*, Removal of indigo carmine (IC) in aqueous solution onto activated pomegranate peel (APP) by adsorption process: Kinetic and thermodynamic studies, *J. Eng. Fibers Fabr.*, 2022, **17**, 15589250211018195.

83 C. Waghmare, *et al.*, Adsorption of methylene blue dye onto phosphoric acid-treated pomegranate peel adsorbent: Kinetic and thermodynamic studies, *Desalin. Water Treat.*, 2024, **318**, 100406.

84 N. Rahman and A. Raheem, Mechanistic investigation of levofloxacin adsorption on Fe (III)-tartaric acid/xanthan gum/graphene oxide/polyacrylamide hydrogel: Box-Behnken design and Taguchi method for optimization, *J. Ind. Eng. Chem.*, 2023, **127**, 110–124.

85 G. Jura and W. D. Harkins, *J. Am. Chem. Soc.*, 1944, **66**, 1356–1362.

 © 2025 The Author(s). Published by the Royal Society of Chemistry